ELSEVIER

HIGHLIGHTED PAPER

RESEARCH: Original Research

Unveiling deformation twin nucleation and growth mechanisms in BCC transition metals and alloys

Jianwei Xiao [1], Lingyu Zhu [1], Rui Wang [1], Chuang Deng [2], Zhaoxuan Wu [1,3,*], Yuntian Zhu [1,3,*]

[1] Department of Materials Science and Engineering, City University of Hong Kong, Hong Kong, China
[2] Department of Mechanical Engineering, University of Manitoba, Winnipeg, MB R3T 5V6, Canada
[3] Hong Kong Institute for Advanced Study, City University of Hong Kong, Hong Kong, China

Twinning provides critical stress-relieving and flaw tolerance in body-centred cubic (BCC) transition metals (TMs) when dislocation plasticity is suppressed. Twin nucleation and growth mechanisms have been studied for over half a century without a consensus. Here, we use a reduced-constraint slip method to unveil the path to twin nucleation, growth and associated energy barriers in the entire BCC TM family. Twinning is surprisingly but essentially controlled by a normalized energy difference η between the hexagonal close-packed (HCP) and BCC structures in elemental TMs, and can be effectively tuned and quantitatively predicted by first-principles calculations in TM alloys. Fracture mechanics theory with η-based barriers enables predictions of critical solute concentrations to activate twinning and reverse ductile-to-brittle transitions in BCC TMs, as demonstrated in WRe alloys. The computational approach provides a unified and quantitative method to predict twinning and a practical tool for rapid screening of alloy compositions ensuring ductile behaviour.

Keywords: BCC transition metals; Deformation twinning; Nucleation and growth; Ductile to brittle transition; Density-functional theory calculations

Introduction

Plastic deformation is essential for materials processing, flaw tolerance and toughening [1]. Dislocation is the primary plastic carrier in nearly all metals and alloys at moderate homologous temperatures. When dislocation plasticity is suppressed or exhausted, twinning provides an alternative deformation mode [2,3]. Deformation twinning is critical in a wide range of materials, including (i) elemental metals and semiconductors; (ii) intermetallic alloys [4]; (iii) twinning-induced plasticity steels [5]; (iv) β-Ti [6] gum metals [7] and (v) emerging compositionally complex alloys [1]. In BCC TMs, deformation twinning is ubiquitous in Fe [8,9], Group VB V [10–13], Nb [14,15], Ta [13,14,16], and Group VIB Cr [17], but is less active in bulk Mo [18–20] and W [21,22]. The twinning behaviour or twinnability is thus distinctly different among these TMs, even though they share the common partially-filled *d*-bands, crystal structure and many other intrinsic properties. The prevalence of deformation twinning is dictated by the twin nucleation mechanism and associated barriers relative to other competing plastic modes such as dislocation glide, phase transformation or fracture. Nucleation typically passes through some unstable transition states at sub-nanometer length scales and over femtosecond time scales, and depends on the fine details of the underlying crystal structure and atomic bonding. Nucleation processes are thus generally intractable in experiments. In BCC TMs, twin nucleation and growth remain not well understood, despite their fundamental importance and intensive research over 70 years [3,23–27].

Multiple twin nucleation mechanisms have been proposed for BCC structures [3,26]. For example, the classical pole mechanism

* Corresponding authors.
E-mail addresses: Wu, Z. (zhaoxuwu@cityu.edu.hk), Zhu, Y. (y.zhu@cityu.edu.hk).

 https://doi.org/10.1016/j.mattod.2023.03.028

[28] requires dissociation of a perfect <111>/2 dislocation, a series of complex cross-slips and an exceedingly high activation stress $\tau_t = \gamma_{us}/b$ [26] (b is the magnitude of the Burgers vector $\mathbf{b}$ = <111>/2 and γ_{us} is the unstable stacking fault (SF) energy). Sleeswyk proposed the core dissociation mechanism where a perfect screw dislocation dissociates into 3 fractional dislocations of <111>/6 which then cross-slips to form a twin embryo with a critical stress of $\tau_t = 3\gamma_{isf}/b$ (γ_{isf} is the intrinsic SF energy). However, these models require complex hypothetical dislocation reactions, highly coordinated atomic motions, or activation stresses at least one order of magnitude higher than that in experiments [26]. In addition, all present models and predictions fail to rationalize the differences among Fe, Group VB and VIB TMs, twinning dependence on temperature, strain-rate and alloy composition, as well as the intrinsic twin and anti-twin behaviour [15].

In this work, we introduce a reduced-constraint (RC) slip path to unveil the twin nucleation and growth mechanisms with density-functional theory (DFT) calculations. In the RC pathway, the twinning barrier γ_t is calculated as a function of slip $\mathbf{s}$ by incrementally displacing all atoms above a slip plane (between layer 6 and 7 in Fig. 1a) by $\delta\mathbf{s} = 0.04\mathbf{b} = 0.02$ <111> in the slip direction, followed by structure optimization with atoms immediately above and below the slip plane fixed in the slip direction and all other degrees of freedom relaxed. Atoms in other layers are fully relaxed during structure optimization. The RC slip is similar to the modified generalized SF energy (GSFE) calculation employed in HCP structures [29,30]. It yields GSFE (γ-lines) close to the classical ones [31] or the generalized planar fault energy lines. However, the structure optimization at each slip increment $\delta\mathbf{s}$ removes excessive constraints and allows multilayer interactions, leading to spontaneous formation of a 2-layer twin embryo in Fe, Group VB TMs, Cr, WRe and MoRe alloys, but not in pure Mo or W. We demonstrate that the RC slip path simulates typical nucleation scenarios, such as at grain boundary (GB) triple junctions and crack tips [32,33] where shear stress is only amplified locally within several atomic layers. Based on the twin nucleation and growth mechanisms, we present a unified model to predict ductile and brittle behaviour at crack-tips applicable to all BCC TMs. The quantitative model reveals (i) the physical origin of twin vs anti-twin; (ii) subtle differences among Fe, Group VB and Group VIB TMs; (iii) change of twinning behaviour via alloying and (iv) a mechanism to reverse the ductile-to-brittle transition (DBT) in BCC TM alloys.

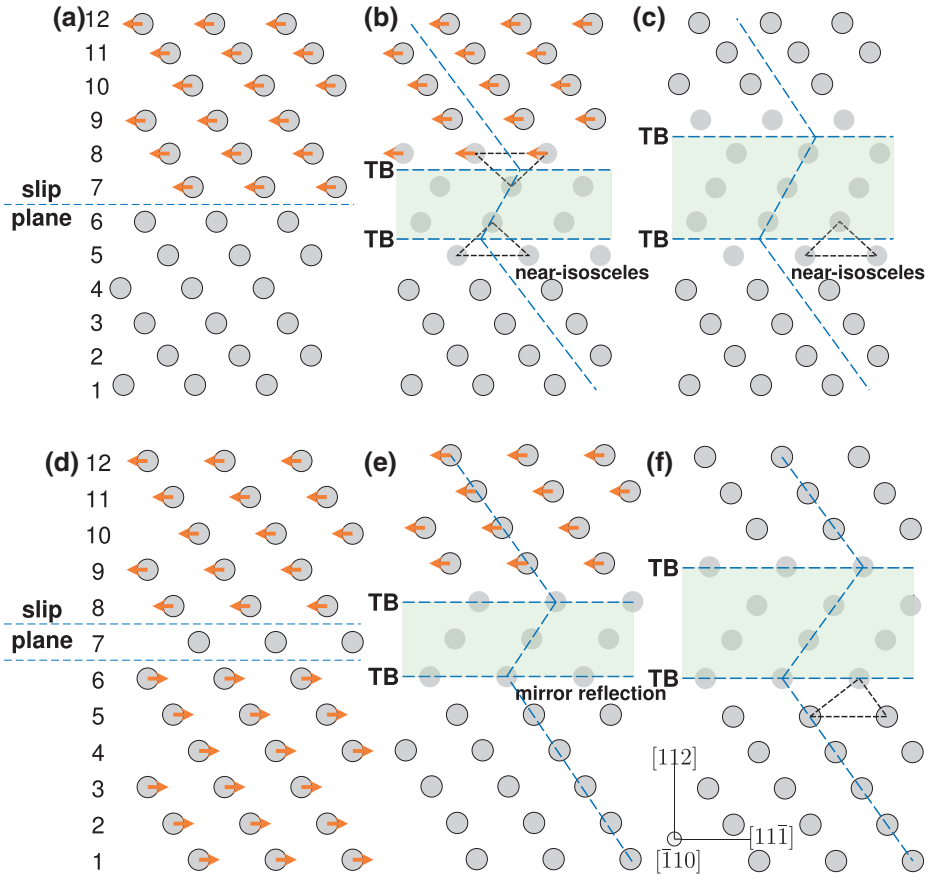

FIGURE 1

Twin nucleation and growth mechanisms in Fe, Group VB and VIB TMs. (a) Homogeneous displacements applied to atoms above the slip plane in the perfect BCC structure. (b) A 2-layer twin embryo following slip of 0.4**b** between layer 6 and 7 in (a) and optimization with atoms in the green box fixed in the slip direction only. (c) Twin growth following slip of 0.2**b** between layer 7 and 8 in (b) and optimization with atoms on layer 7 and 8 fixed in the slip direction only. (d) Homogeneous displacements applied to atoms above and below 2 slip planes in the perfect BCC structure. (e) A 3-layer twin embryo following slip of 0.33**b** between layer 6 and 7, and between layer 7 and 8 in (d). The structure is optimized with atoms on layer 6 and 7, 7 and 8 fixed in the slip direction. (f) Twin growth following slip of 0.33**b** between layer 8 and 9 in (e).

Results and discussion

Twinning and dislocation slip in BCC Fe

Fig. 2 shows the respective γ-lines of Fe along the $\langle \bar{1}\,\bar{1}\,1 \rangle$ direction on {112} twinning plane computed by DFT with the standard and RC methods (see SI). We denote the slip direction as x, normal to the slip direction in the slip plane as y, and slip plane normal z. The fully constrained $\gamma_{\text{fix-x-y-z}}$-line is asymmetric, has no meta-stable point and reaches peak at slip $\mathbf{s}_d \approx 0.55\mathbf{b}$. The $\gamma_{\text{fix-x}}$-line, which allows ionic optimization in y and z, has a similar profile with its peak energy reduced by 17%. The γ_{rc}-line, calculated by the RC method, also has a similar profile at both ends of the slip, but exhibits (i) a meta-stable SF at slip $\mathbf{s}_c \approx 0.4\mathbf{b}$ and (ii) a further reduced peak energy γ_{ud} required for the nucleation of a full dislocation (see SI). At the meta-stable point $\mathbf{s}_c$, a 2-layer twin is formed spontaneously with excessive energy γ_{2tw} (Fig. 1b and Table S2). The formed 2-layer twin is stable and its configuration is identical to the fully relaxed structure obtained by optimization with all ionic constraints removed.

The twin boundaries (TBs) enclosing the 2-layer twin have similar structures and energies as the fully-grown TBs (Fig. S3). Specifically, the twin structure does not possess a mirror reflection symmetry, but has a near-isosceles structure with a finite translation $\boldsymbol{\delta}$ in the twin direction and some distortions on the TBs (Table S2). This near-isosceles TB is the ground state structure with an energy $\gamma_{\text{iso-tw}}$ = 0.418 J/m^2, 0.03 J/m^2 lower than the meta-stable reflection symmetry TB.

The 2-layer twin nucleus can grow by applying a slip $\delta\mathbf{s}$ again on atoms above the top TB (layer 8 and above in Fig. 1b), followed by structure optimization with the 2 layers of atoms above and below the TB (layer 7 and 8) fixed in the slip direction. The slip can be applied in the twin and anti-twin directions, yielding drastically different energy variations and barriers $\gamma_{\text{utw-t}}$ and $\gamma_{\text{utw-at}}$ (Fig. 2). In the twin direction, the barrier to growth is $\gamma_{\text{utw-t}} - \gamma_{2tw}$ = 0.031 J/m^2, which is negligible compared to $\gamma_{\text{utw-at}} - \gamma_{2tw}$ = 0.514 J/m^2 in the anti-twin direction. Further twin growth, from 3 layers to 4 layers and so on, incurs barriers of similar magnitudes. Furthermore, the total barrier to twinning $\gamma_{\text{utw-t}}$ is 16% lower than γ_{ud} while $\gamma_{\text{utw-at}}$ is 37% higher than γ_{ud}; nucleation and growth of a twin is thus predicted to be more favourable than that of a full dislocation in the twin direction and less favourable in the anti-twin direction. Compressive loadings in the <001> and <110> directions create shear stresses in the anti-twin and twin directions, which naturally activate dislocation plasticity and twinning, respectively (Fig. 2). The above energetics and predictions are fully consistent with twinning or dislocation plasticity in experiments of single crystal Fe [34,35], Nb [15], Ta [16], Cr [17] and atomistic simulations in Fe [36].

Twinning and dislocation slip in the BCC TM family

The RC slip reveals the twin nucleation and growth mechanisms and associated barriers in BCC Fe. It can be applied to other Group VB and VIB TMs. Fig. 3 shows the γ-lines of 6 BCC TMs computed using DFT. The standard $\gamma_{\text{fix-x}}$-lines have similar features among the elements; all peak between 0.5–0.6$\mathbf{b}$ without any meta-stable fault as that in Fe. In contrast, the γ_{rc}-lines exhibit distinct differences among the 6 cases; Group VB (V, Nb, Ta) show shallow energy valleys with meta-stable faults at $\mathbf{s}_c \approx 0.4\mathbf{b}$ similar to Fe, Cr has a brief energy drop and a meta-stable fault at a similar location as Group VB, while Mo and W do not have any meta-stable fault and their γ_{rc}-lines are nearly identical to the

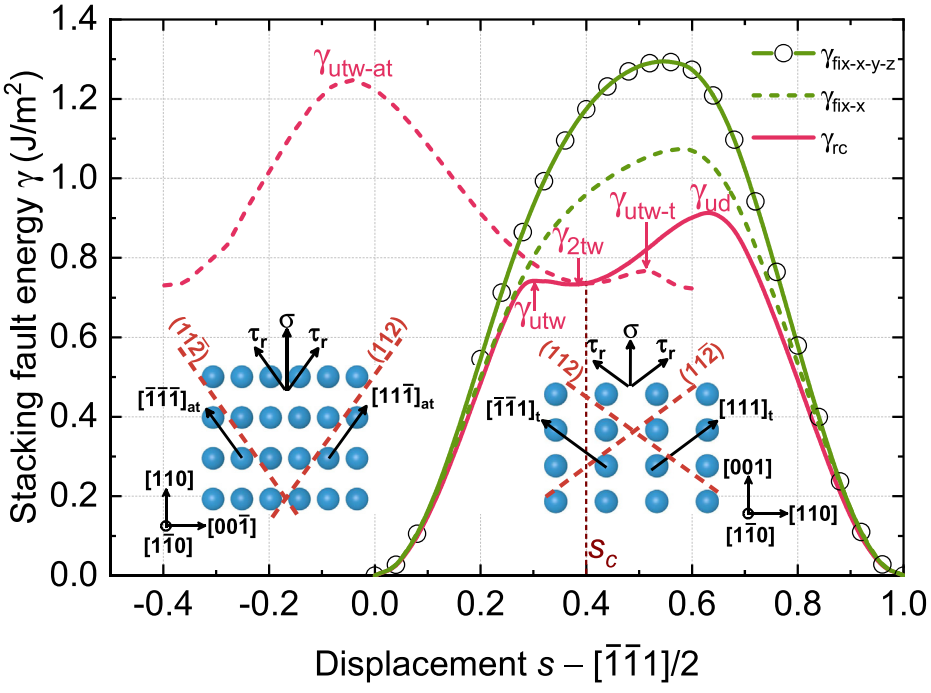

FIGURE 2

Generalized SF energy (γ-lines) on the {112} plane of BCC Fe calculated by DFT. The green solid and dashed lines are calculated with full atomic constraints and atomic constraints in the slip direction. The magenta solid line is the γ_{rc}-line calculated by the RC method. The magenta dashed line shows the energy variations to twin growth in the twin and anti-twin directions.

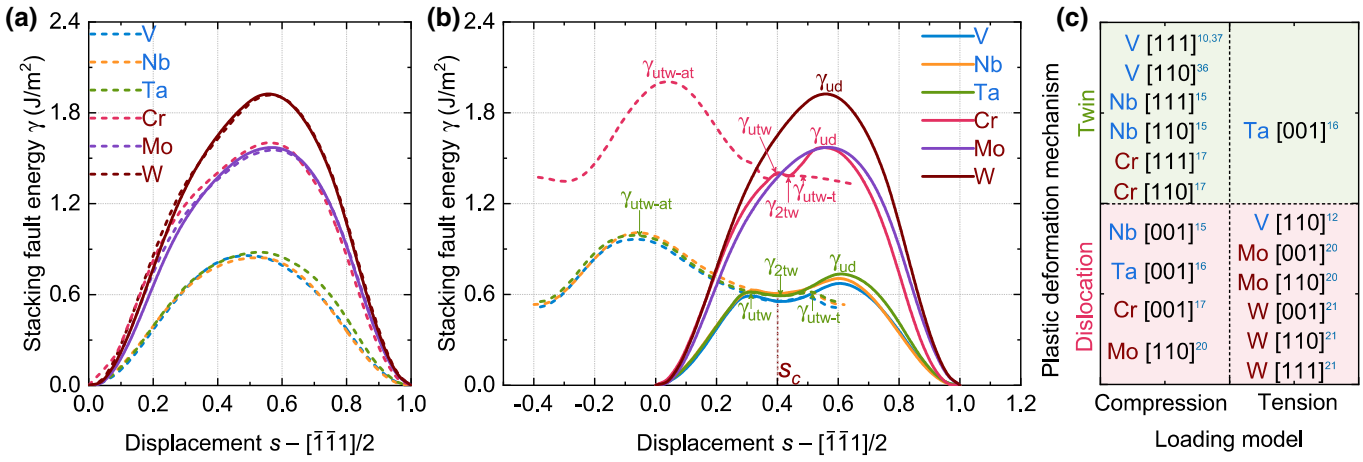

FIGURE 3

Generalized SF energies (γ-lines) on the {112} plane of Group VB and VIB TMs calculated by DFT. (a) The dashed lines are the $\gamma_{fix\text{-}x}$-lines and the solid lines are the γ_{rc}-lines of Mo and W superimposed. (b) γ_{rc}-lines of 6 TMs. The dashed lines are the energy barrier for twin growth in the twin and anti-twin direction. (c) Deformation mechanism in tension and compression of single crystal experiments. Deformation twinning is activated only when the resolved shear stress is in the twin direction and dislocation mechanism is activated when shear is in the anti-twin direction.

respective $\gamma_{fix\text{-}x}$-lines (Fig. 3a and b). Similar to Fe, a 2-layer twin is formed spontaneously in Cr (grows to 4 layers) and Group VB TMs upon structure optimization at $\mathbf{s}_c$ (Fig. 1a-b) and with an excessive energy γ_{2tw} (Table S2), while no twin structure is formed in Mo and W. All the formed twin structures are stable in subsequent structure optimization with all atomic constraints removed. The TBs enclosing the 2-layer twin have similar structures and energies as the fully-grown TBs. The magnitude of $\boldsymbol{\delta}$ differs quantitatively among the elements (Table S2). The near-isosceles TB structure is the ground state structure in Group VB TMs, but is meta-stable in Cr with respect to the reflection structure and unstable in Mo and W. In the RC slip process, the presence of the stable/meta-stable faults characterized by $\boldsymbol{\delta}$ and the 2-layer twin is fully consistent with the activation of deformation twinning reported in bulk Fe and these 6 BCC TMs. In particular, deformation twinning and TB with translation $\boldsymbol{\delta}$ are widely observed in Fe [34,35], V [10,12,37,38], Nb [15], Ta [16], Cr [17], but not common in bulk Mo [19,20] or W [21] under quasistatic tensile loadings.

In the 4 TMs with a stable/meta-stable 2-layer twin, the barriers to growth are $\gamma_{utw\text{-}t} - \gamma_{2tw} \in 0.001\text{–}0.029$ J/m^2 and $\gamma_{utw\text{-}at} - \gamma_{2tw} \in 0.398\text{–}0.721$ J/m^2 in the twin and anti-twin directions, respectively. From the 2-layer twin embryo, twin growth can occur easily in the twin direction but faces high energy barriers in the anti-twin direction, again similar to the case in Fe. We envision another scenario where the RC slip is applied in the anti-twin direction and passes the highest barrier γ_{ud}, a full <111>/2 dislocation is expected based on established dislocation theory [39]. Even a 2-layer twin can be formed at $\mathbf{s}_c$ after passing through γ_{ud}, growth in the anti-twin direction is still nearly impossible given the high energy barrier $\gamma_{utw\text{-}at} - \gamma_{2tw}$, which is much larger than $\gamma_{utw} - \gamma_{2tw}$ for forming the full dislocation. Therefore, deformation twinning in the anti-twin direction is unlikely in all the 5 BCC elements exhibiting twinning behaviour, consistent with all single crystal experiments shown in Fig. 3c.

For Mo and W, the above RC slip does not lead to the formation of twin structures. However, a 3-layer twin can be formed spontaneously by applying the slip twice on atoms above and below 2 consecutive slip planes. Specifically, we first apply $\mathbf{s}_c \approx 0.33\mathbf{b}$ to all atoms above a selected slip plane (layer 8–12 in Fig. 1d), followed by a second $\mathbf{s}_c$ to all atoms below a second slip plane (layer 1–6 in Fig. 1d). The slipped structure is optimized with three layers of atoms (layer 6, 7, 8) fixed in the slip direction, which results in a 3-layer twin structure (Fig. 1e). The formed 3-layer twin has a mirror symmetry with structures and energies similar to the fully grown twins (Fig. S5e-f). Subsequent twin growth can occur following the same process as that in the Group VB TMs and Cr (Fig. 1f). The mechanism to form the 3-layer twin is difficult in practice, since the 2-layer twin, on which the 2nd slip rests, is not even meta-stable. Twinning is thus more difficult in Mo and W than in other TMs examined here. Therefore, the stable/meta-stable isosceles TB structures are crucial and dictate twin nucleation. The meta-stable SFs on the γ_{rc}-lines manifest their existence.

Twinning disconnection and twin growth

In Group VB TMs, Cr and Fe, the presence of the isosceles and reflection TB structures has important consequences on the TB disconnection and the true twin growth process, similar to the meta-stable SF and partial dislocation glides in regular crystal lattices (e.g., Shockley partials in FCC). Twin grows via the migration of the TB, which is carried out by the glide of a disconnection possessing a Burgers vector $\mathbf{b}_{td}$ and a step character $\mathbf{h}_{td}$. The TB disconnection can be analysed with established bicrystallography. Specifically, a dichromatic pattern can be formed by extending the twin and matrix lattices over the entire space (Fig. 4). From the dichromatic pattern, a displacement shift complete (DSC) lattice can be generated and gives all possible translation vectors preserving the symmetry relation of the two lattices (Fig. 4d). The DSC lattice depends on the displacement $\boldsymbol{\delta}$, so do the permissible disconnection Burgers vectors at the TBs. In the general case where $\boldsymbol{\delta} \neq 0$, two translation vectors parallel to the TB, $\boldsymbol{\delta}$ and $\boldsymbol{\beta}$, can be identified and satisfy the condition of $\boldsymbol{\delta} + \boldsymbol{\beta} = \mathbf{b}_t = <111>/6$. These two vectors give the Burgers vectors of the disconnections on the TB. In Fe, Group VB TMs and Cr,

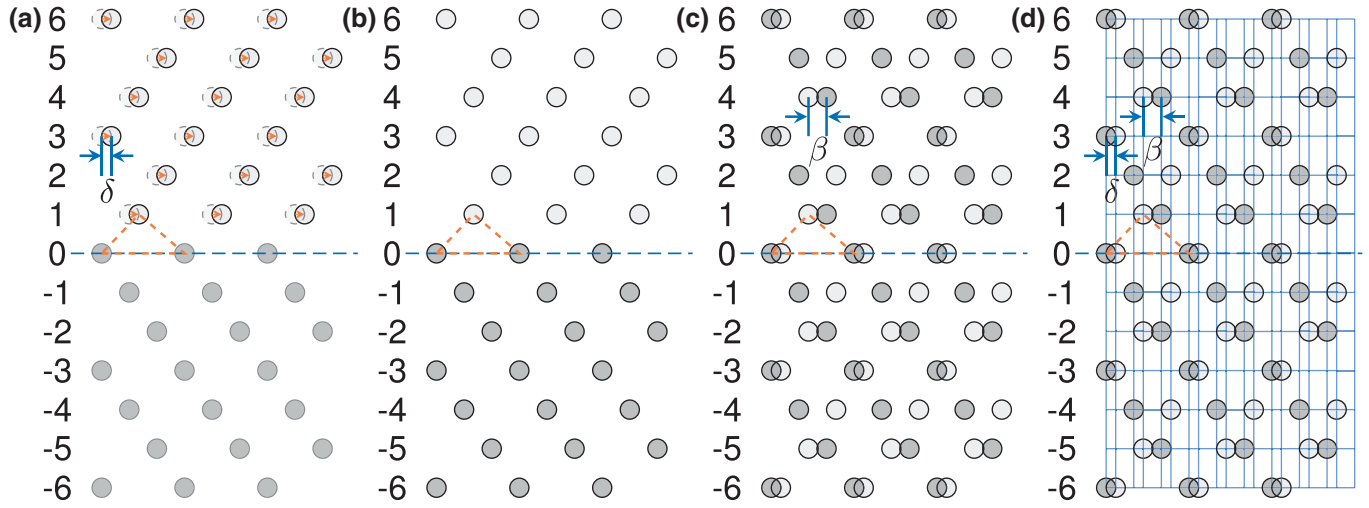

FIGURE 4

Dichromatic patterns for {112} <111> TB structure with the DSC lattice showing the two possible Burgers vectors $\boldsymbol{\delta}$ and $\boldsymbol{\beta}$ parallel to the TB. (a) The formation of the near-isosceles TB structure from the mirror reflection TB (dashed circles) plus finite displacement $\boldsymbol{\delta}$. (b) The near-isosceles TB structure. (c) Dichromatic pattern formed by extending the matrix and twin lattices across the TB. (d) DSC lattice of the near-isosceles twin-matrix structure. In all figures, the gray circles represent atoms in the matrix and the white circles represent atoms in the twin.

the TB disconnection is thus predicted to be partial disconnections of Burgers vector $\boldsymbol{\delta}$ and $\boldsymbol{\beta}$, and separated by a TB SF of energy γ_{tbsf} in between (Table S2). TB migration is carried out separately by these partial disconnections. In Mo and W, the TB disconnection is predicted to have a Burgers vector of $\mathbf{b}_t$ ($\boldsymbol{\delta}$ = 0), identical to the twinning Burgers vector. The TB structure and twin growth are thus distinctly different among the TM family.

Direct validation on nucleation and growth mechanisms

In the above twin nucleation mechanism, the RC slip is critical but still requires hypothetical atomic displacements to activate the nucleation process. The growth mechanism via partial disconnections is also built upon bicrystallography without energetic considerations. They only offer possible mechanisms for twin nucleation and growth in BCC structures. We thus verify both mechanisms in direct atomistic simulations. We simulate twin nucleation at the tip of a Griffith crack on the (112) plane with the crack front in the $\left[\bar{1}\,10\right]$ direction and under mode-I loading in BCC V (Fig. 5a and SI). With increasing loading, shear deformation increases along the $\left(\bar{1}\,\bar{1}\,2\right)$ plane under the crack-tip stress field. Slip is particularly localized within two layers of atoms at the crack tip (Fig. 5b). At the critical loading (ε_{yy} = 4.55%), a twin nucleus is formed and quickly grows into multiple layers (Fig. 5c). At the twin tip, twin propagation is led by a 2-layer twin structure identical to that obtained via the RC slip method in DFT (Fig. 1b). Twin growth or thickening is carried out by a pair of disconnections with Burgers vector $\boldsymbol{\delta}$ and $\boldsymbol{\beta}$ separated by a TB SF, as predicted in the analysis using the DSC lattice. In particular, twin growth follows immediately upon the nucleation of the 2-layer twin embryo, consistent with the low growth barrier predicted by the γ_{rc}-line in the twin direction (Fig. 3).

The simulation thus provides an explicit validation on the proposed twin nucleation and growth mechanisms in BCC V. Separately, the critical stress intensity factors (SIFs) can be predicted using linear elastic fracture mechanics (LEFM) for the respective deformation modes, i.e., twinning, dislocation emission and cleavage (Method and SI). For twin nucleation, we use γ_{utw} and predict the critical SIF K_{It} as 0.66–0.82 MPa $m^{1/2}$, close to the actual value 0.6 MPa $m^{1/2}$ in the simulation and lower than K_{Ic} for cleavage (SI). For dislocation emission, we use γ_{ud} and the critical SIF K_{Ie} is predicted to be 0.7–0.85 MPa $m^{1/2}$, higher than K_{It} but lower than K_{Ic}, indicating dislocation emis-

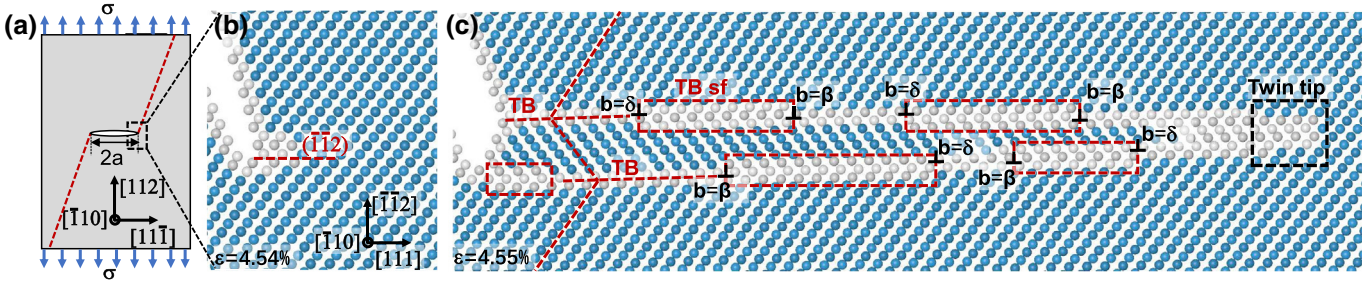

FIGURE 5

Twin nucleation and propagation at the tip of a Griffith crack. (a) Schematic of the simulation model. (b) Atomic configuration at the crack tip at the critical loading. (c) Twin nucleation and growth with a 2-layer twin embryo at the tip and partial TB disconnections and SF.

sion is also more favourable than cleavage. LEFM theory thus predicts that twinning should occur prior dislocation emission and cleavage, in agreement with the direction simulation where twinning is activated and blunts the $\{112\}\left[\bar{1}\,10\right]$ sharp crack tip, relieving the stress concentration and leading to ductile behaviour in this crack orientation (Fig. S6).

Twinning in WRe alloys and DBT

Group VIB Cr exhibits a brief energy drop at $\mathbf{s}_c$, which leads to the critical 2-layer twin formation. It is surprising that Mo and W in the same group do not possess such features even though they share similar electronic structures. On the other hand, experiments show that twinning is activated upon Re addition in W and Mo binary solid solution alloys [40–42]. We reveal the Re effects on twin activation in these alloys using DFT again. Fig. 6 shows the respective γ_{rc}-lines of WRe average alloys calculated using the RC slip method and virtual crystal approximation (VCA [43], see SI). Similar to results in previous studies [44], Re reduces the γ-lines at all concentrations for W. At 10 at.%Re, the γ_{rc}-line has a similar profile as that of Cr, with a brief drop in energy/metastable fault at $\mathbf{s}_c \approx 0.4\mathbf{b}$. At $\mathbf{s}_c$, a 2-layer twin is formed spontaneously during structure optimization with or without constraints (Fig. 1b). With further increasing Re concentration c, the positions of the meta-stable fault $\mathbf{s}_c$ and critical barrier for twinning γ_{utw} shift to the left, and the γ_{rc}-lines are further lowered and approach those of Group VB TMs and Fe. In these alloys, a 2-layer isosceles twin structure, similar to that in Fe, Cr and Group VB TMs, is formed spontaneously at $\mathbf{s}_c \approx 0.4\mathbf{b}$ (Fig. 1b). At $\mathbf{s}_c \approx 0.34, 0.36, 0.38\mathbf{b}$, a 4-layer twin of mirror reflection is formed (Fig. 1f). The mirror reflection TB structure has a lower energy than the isosceles TB. In all the cases, the positions of peak value γ_{ud}, corresponding to the barrier to a full dislocation nucleation, remain nearly the same at $\mathbf{s}_c \approx 0.55\mathbf{b}$.

Quantitatively, γ_{ud} scales linearly with c in the entire range, while γ_{utw} first appears at 10 at.%Re, drops rapidly up to 25 at.%Re, and followed by linear scaling afterwards (Fig. 6b). Reduction in γ_{utw} or γ_{ud} favours twin or dislocation nucleation over

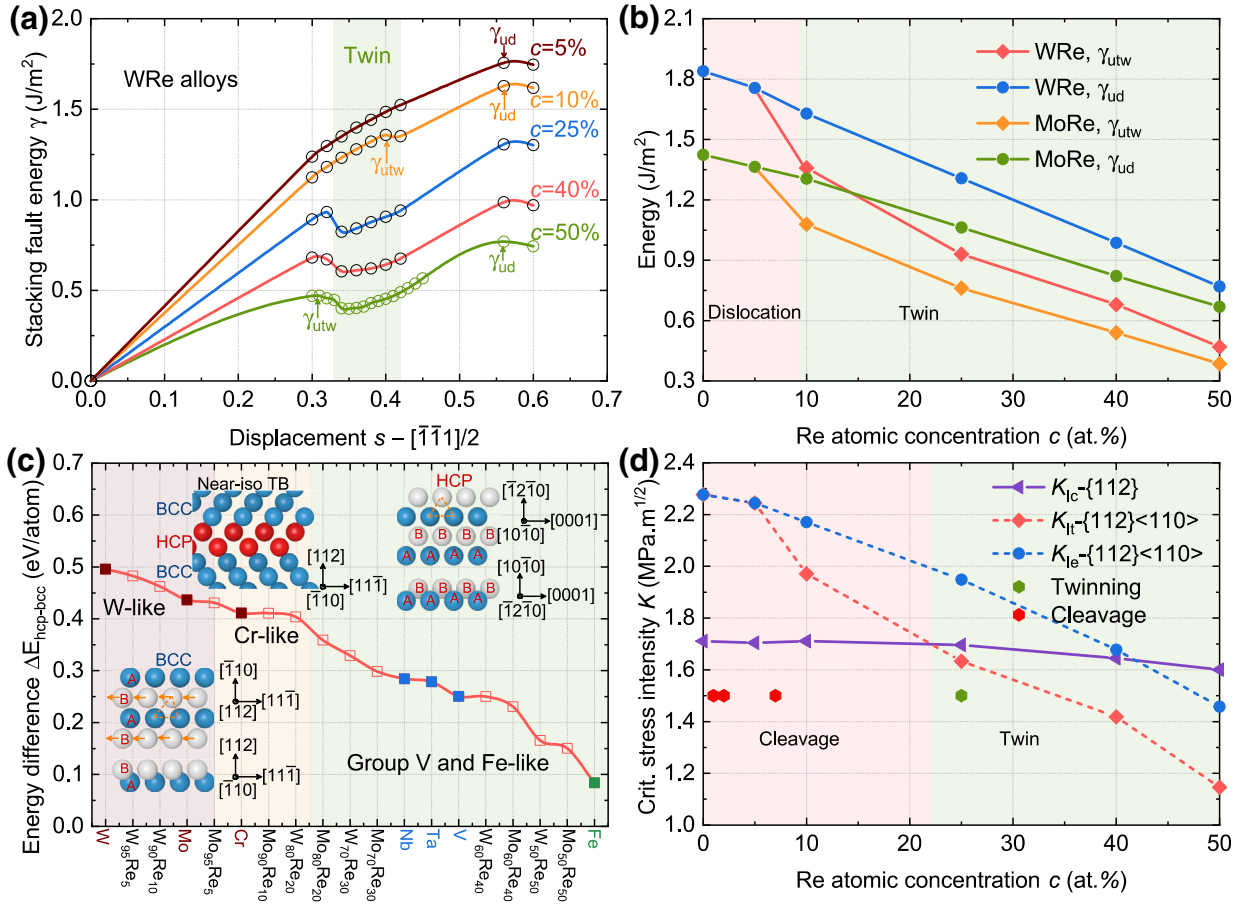

FIGURE 6

Re effects on material properties of binary WRe and MoRe solid solution alloys calculated by DFT. (a) γ_{rc}-lines as a function of Re concentration in WRe. (b) Twin and dislocation nucleation barriers as a function of Re concentration in WRe and MoRe alloys. (c) Energy difference between the HCP and BCC structures in elemental TMs and alloys. In the lower left inset, white atoms on a {112} plane slip to $\mathbf{s}_c$, forming the near-isosceles (dashed triangle in orange) TB with a local structure resembling the HCP structure (upper right). (d) Critical SIFs for twinning (K_{It}), dislocation emission (K_{Ie}) and cleavage (K_{Ic}) at a (112) $\left[1\,10\right]$ sharp crack tip under mode-I loading as a function of Re concentration in WRe alloys. The red and green dots show cleavage and twinning observed in low and high Re concentrations respectively in binary WRe alloy experiment [41].

brittle cleavage, which is the primary toughness limiting factor in W below its DBT temperatures [45]. In pure W, cleavage is predicted for sharp cracks on the low-index ({100}, {110}) planes, as SIFs K_{Ic} for cleavage are much lower than K_{Ie} for dislocation emission (Fig. S13). At 10 at.%Re and above, twinning can be activated with lower energy barriers γ_{utw} than γ_{ud} for dislocation emission. Above this threshold concentration, K_{It} is always lower than K_{Ie}. For the {100}<110>, {110}<110> and {112}<110> sharp cracks under mode I loading, K_{It} becomes lower than K_{Ic} at critical concentrations c_{crit} = 48, 28 and 22 at.%, respectively (Fig. 6d and S14). The latter two concentrations are close to the Re concentrations used in many commercial WRe alloys. Sufficient Re addition can thus turn intrinsically brittle cleavage in pure bulk W into ductile twin deformation in WRe alloys via a mechanism similar to that in V shown in Fig. 5. In this case, twinning should be absent in pure bulk W and prevalent in WRe alloys when Re concentrations reach 20–30 at.%. This prediction is consistent with (i) cleavage fracture in pure W and dilute WRe alloys without twinning [46]; and (ii) twinning deformation at GBs and crack tips in a W-25at.%Re alloy deformed at room temperature [41].

On the other hand, cleavage always occurs prior dislocation emission based on predictions of K_{Ie} with γ_{us} on the standard γ-lines at all Re concentrations [44,47]. WRe alloys would thus still be intrinsically brittle, which contradicts the presence of stable, non-propagating micro-cracks in W-25at.%Re alloys [41]. The RC slip method employed here thus reveals the twinning mechanism and enables quantitative predictions of critical concentration for twinning and ductilization at crack tips in BCC structures. The findings of twinning mechanism and critical Re concentrations close the long-standing gap between theoretical prediction of brittle cleavage and experimental observation of ductile plastic deformation in WRe alloys [47]. It also provides a mechanism to reverse or delay the DBT in brittle materials such as W when dislocation plasticity is suppressed (e.g., by high lattice frictions at low temperatures or strengtheners such as solutes and precipitates) and local stresses reach levels capable of driving crack nucleation and propagation.

Extension and discussion on the physical origin

The activation of twinning via Re solutes in W demonstrates a general mechanism to blunt sharp cracks and hence arrest their fast propagations required in all BCC TMs (Fig. S13). Fig. 6b further predicts that twinning can potentially be activated at crack tips in MoRe alloys with Re concentrations above 10 at.%. This is consistent with early experiments where twinning was observed in Mo-18at.%Re deformed at 77 K and was profuse in Mo-(34–35)at.%Re deformed at room temperatures [40,42,48]. The prediction also shows that Re reduces the barrier to twin nucleation in Mo, which is again consistent with the decrease of critical stresses for twinning observed in experiments [48]. We note that twinning or dislocation emission is not predicted at mode-I crack tips in pure Mo (Fig. S13). Nevertheless, twin were found adjacent to propagating cracks under tensile loading [48]. The origin for this discrepancy is not entirely clear. At least two factors could contribute to this discrepancy: (i) the crack could be advancing at considerable speeds, i.e., under dynamic fracture conditions, which change the crack tip field and behaviour; (ii) the γ-lines could be further reduced when normal stresses are taken into considerations (discussed below), as seen in the atomistic simulations above (SI). Overall, the low-index plane cracks in pure Mo are still intrinsically brittle; solutes such as Re are required to change them to semi-brittle or ductile.

Finally, we discuss the physical origin governing deformation twinning in all the above cases. Essentially, twinning is driven by slip in the <111> direction on the {112} planes, which passes through a configuration with stacking sequence similar to that of the hexagonal close-packed (HCP) structure (see insets in Fig. 6c). Unlike the SF in FCC structures, the SF here is not exactly HCP, but only resembles its local atomic environments. We relate the meta-stable SF energy to ΔE defined as the energy of the HCP structure relative to the ground state BCC structure. While this relation is not exact, it offers a simple criterion to differentiate the subtle differences among the TM family and alloying effects. We show that ΔE gives a general trend consistent with the presence of a meta-stable SF/twin embryo, which ultimately has a quantum mechanics electronic origin. In pure Mo and W, $\Delta E \approx 0.45$ eV/atom, and is the largest among all cases (Fig. 6c). Alloying with Re first decreases ΔE towards that of pure Cr, making the HCP structure less unfavourable. With Re above some critical concentrations (10 at.% for W and Mo), an HCP-like structure, manifested as the near-isosceles TB structure, is spontaneously formed at $\mathbf{s}_c$ on the RC slip path and accompanied by the appearance of a meta-stable fault on γ_{rc}-lines. Further increasing Re concentrations reduces ΔE towards that of Group VB TMs and finally Fe. Smooth decrease of ΔE with increasing Re concentration corroborates continuous evolution of γ_{rc}-line profiles from pure W-like to Cr-like, and finally to Group VB and Fe-like (Fig. 6a and c).

For WRe and MoRe alloys, both the barrier to twinning γ_{utw} and the barrier to dislocation nucleation γ_{ud} can be quantitatively related to ΔE, which in turn is controlled by Re concentrations. Specifically, in solid solution average WRe alloys above the threshold concentration, γ_{utw} can be approximated as

$$\gamma^{A}_{utw}(\eta) = \gamma^{C}_{utw}[1 + k_{utw}(\eta - 1)]; \eta = \Delta E^{A}/\Delta E^{C}, \quad (1)$$

where γ^{C}_{utw} is the barrier to twin nucleation at the threshold concentration, ΔE^{A} and ΔE^{C} are the energy differences at the threshold concentration and the concentration in the actual alloy, and k_{utw} = 1.06 is the scaling factor fit from the data (Fig. S16). The normalizing index η has a similar functional form of the material index χ controlling dislocation properties [44]. Both η and χ are ultimately related to the valence electron concentration in the alloy, so do γ^{C}_{utw} and γ_{ud}. All physical quantities and binary average alloying effects can thus be computed rapidly using first-principles DFT, which enables predictions of K_{It}, K_{Ie} and K_{Ic} dictating material intrinsic ductile/brittle behaviour, as demonstrated in the WRe case.

The prediction on twinning and associated properties can be extended to the entire BCC TM family and binary alloys, similar to that of χ for dislocation properties. For example, pure V is on the boundary between intrinsically brittle and ductile behaviours (Fig. S13); alloying V with Ti (or solutes on the left of Group VB) at moderate concentrations is expected to reduce γ_{utw} and shift V to the ductile side completely. Alloying Nb with Zr continuously

reduces $\Delta E/\eta$ (Fig. S17) and twinning barrier γ_{utw}, which favours deformation twinning; this prediction is consistent with experiments where twinning is even activated above room temperature at 25 at.%Zr concentration [49]. For group VB TMs, solutes on their right are expected to raise ΔE, γ_{utw} and reduce twinnability, as shown in Fig. S17 for binary TaRe alloys and consistent with experiments [16]. For all Group VIB TMs, the gap between brittle cleavage and ductile twinning is relatively large and ductilization requires Re (or solutes on the right of Group VIB) at high concentrations (e.g., 25 at.%). For Cr, $\Delta E/\eta$ is reduced with Re solutes (Fig. S17), which reduces twinning barrier and increases twinnability, consistent with earlier experiments where twinning is enhanced, microcracking is suppressed and DBT temperature is decreased significantly at high Re concentrations (e.g., 36 at.%Re [50]). The Re effect in Cr is similar to that in MoRe/WRe alloys. Separately, CPA-DFT calculations [51] show that Fe can substantially reduce ΔE and thus twinning barrier γ^{A}_{utw} relative to pure Cr (Fig. S18), which is in agreement with reduced GSFE γ-line calculated for Fe-50at.%Cr [52] and twinning deformation even at elevated temperatures in Cr-32at.%Fe [53] and Cr-48at.%Fe [54]. Furthermore, Fe is also shown to exhibit solute dependent twinning (e.g., Fe-6.5wt.%Si [55–57]). Solute effects on γ-line and ΔE can also be determined but require consideration of magnetism in Fe. Such calculations are thus more delicate and will be studied separately, given the technological importance of Fe. Overall, the two indices χ and η, introduced in a previous work [44] and the current work here, thus quantitatively and succinctly captures the physical origins governing the two fundamental deformation mechanisms in the entire BCC TM family.

Separately, twinning is reported in deformation of W nanocrystals [58], Mo thin film [59], and at advancing cracks in Mo bulk [18]. The current RC slip path, however, suggests twin nucleation is difficult in these two elements. This apparent discrepancy can be resolved by considering the normal-stress-dependent generalized stacking fault enthalpy (GSFH). Briefly, very-high compressive and tensile stresses can change the general profiles of GSFH lines; the former stabilizes the 2-layer twin embryo while the latter induces a double-peak in the critical stresses for twinning [60]. Both scenarios occur at very high stresses achievable in nanocrystals or at crack-tips during crack propagation. In addition, twinning is generally more prevalent at low temperatures. Multiple factors could contribute to this temperature-dependent behaviour. At high temperatures, dislocations tend to have high mobilities. Their easy-glides relieve local stress concentrations and replace deformation twinning during yielding or plastic flow. On the other hand, the generalized SF free energy should be considered. The energy difference ΔE should be replaced by the free energy difference $\Delta G = \Delta E - T\,\Delta S$. The entropy difference ΔS between the HCP and BCC structure can influence ΔG and the overall GSFE profiles. In non-magnetic elements such as those in Group VB, vibrational entropy may be the dominant contribution to entropy and the HCP structure is expected to have lower vibrational entropy than the BCC structure. In these elements, we expect $\Delta S < 0$. With increasing temperatures, ΔG would thus increase. The energy valley at the meta-stable SF position (Fig. 3b) may become shallower and eventually disappear at high temperatures. The loss of the meta-stable SF eliminates the formation of the 2-layer twin embryo, making dislocation emission the preferential nucleation mechanism under local shear conditions. In Fe and Cr, magnetism could add further complications to ΔG and the activation of twinning. Predictions at finite temperatures thus require further detailed and quantitative study.

Summary

In summary, the reduced-constraint slip method reveals and differentiates the twin nucleation and growth path, associated twin boundary structure and energetics in the entire BCC TM family. Within the family, the twin nucleation and growth mechanisms depend on the presence of the near-isosceles twin boundary structure, which in turn is dictated by the energy difference between the HCP and BCC structures of the metal or average alloy. This critical energy difference can be reduced to a normalizing index η which can be effectively tuned via solid solution alloying and predicted easily for average alloys. Application of the method to WRe alloys with linear elastic fracture mechanics theory leads to quantitative prediction of critical solute concentrations enabling ductile behaviour in otherwise brittle BCC metals. The quantitative prediction closes the gap between theory and experiment on ductile-to-brittle transition in BCC W upon alloying with Re. This mechanism-based, computational approach, with η as the only composition-sensitive input, provides a bottom line criterion for ductile/brittle behaviour in BCC metals and alloys. While the current VCA-based prediction does not capture local solute effects on nucleation barriers, it does provide a practical tool for rapid screening of alloy compositions favouring towards the ductile side and enhanced material toughness. When favourable solute types and concentrations are identified, more detailed calculations and experimental validations can be performed. The current result is mechanism-based and established on crystal geometry and atomic bonding. It is expected to be robust and applicable to all BCC structures in general.

Methods

DFT calculations

The DFT calculations are performed using the Vienna *Ab initio* Simulation Package (VASP [61,62]). Generalized gradient approximation (GGA) functionals in the Perdew-Burke-Ernzerhof (PBE [63]) form are used to describe the exchange and correlation interactions. In each element, the core electrons are replaced by the projector augmented wave (PAW [64]) pseudopotentials and the valence states are shown in Table S1. The cutoff energy of the plane-wave basis set is 520 eV and a first-order Methfessel-Paxton method [65] with a width of 0.1 eV is used to smooth the partial electron occupancies. The Monkhorst-pack *k*-point mesh [66] is used to sample the Brillouin zone with linear *k*-point spacing of ~0.2 $Å^{-1}$. Convergence is assumed when the total energy variation drops below 10^{-5} eV and all the ionic forces are below 0.01 eV/Å. Spin-polarized DFT is used for calculations of Fe and Cr.

In the DFT-VCA [43] calculations, virtual atoms are created with core and valence electrons constructed based on alloy constituents. For each binary $A_{1-x}Re_x$ (A = Cr, Mo or W) alloy, the valence electron number and pseudopotential for core electrons

are formed using that of the respective constituent elements weighted by their atomic fractions. All other parameters in DFT-VCA are the same as that in the standard DFT calculations.

In the BCC structure, the generalized SF energy γ-lines in the <111> direction on the {112} plane are calculated using slab-vacuum supercells. Specifically, the supercells contain 12 and 16 {112}-plane atomic layers for pure BCC metals and binary $A_{1-x}Re_x$ alloys, respectively. In all the cases, the vacuum layer thickness is ~15 Å.

Molecular dynamics simulations

A Griffith crack under mode-I loading is simulated using the Large-scale Atomic/Molecular Massively Parallel Simulator (LAMMPS [67]). We use a supercell of perfect BCC crystal with its crystallographic direction $\left[11\bar{1}\right]$ oriented along the *x*-axis, [112] along the *y*-axis, $\left[\bar{1}10\right]$ along the *z*-axis (Fig. 5a). The crystal has a dimension $2W \times 2H \times t = 40$ nm $\times$ 25 nm $\times$ 2 nm. Periodic boundary conditions are imposed in all directions. A {112} <110> crack of length $2a$ = 5.2 nm is created at the center of the supercell with the crack plane normal in the *y*-direction and crack front in the *z*-direction (Fig. S6). Traction-free crack surfaces are realized by cancelling interatomic interactions between atoms on either side of the crack plane within the crack length $2a$. The system with the crack is quasi-statically loaded in the *y*-direction by applying an incremental strain $\varepsilon_{yy} = 0.001$, followed by structure optimization using the conjugate gradient algorithm with stress-free conditions maintained in the *x*-direction and the thickness in the *z*-direction kept constant throughout the loading process. Convergence is assumed when all forces on atoms drop below 10^{-4} eV/Å. The critical event at the crack tip (cleavage, dislocation or twin nucleation) is not sensitive to the loading step size, structure optimization details and boundary conditions, as is well known in established fracture mechanics theory.

Interatomic interactions are described by an extended modified embedded-atom method (XMEAM) potential for BCC V [68] (SI). This XMEAM potential for V (V1) reproduces nearly all lattice and defect properties at DFT accuracies. In particular, V1 has accurate surface energies when compared to DFT values. For the {100}, {110}, {112}, {123} planes, the discrepancies are 11%, 2%, 0.4%, 0.8%, respectively. It also possesses accurate γ-lines with the unstable SF energy γ_{us} within 5% from the DFT values on the {110}, {112} and {113} slip planes. V1 also possesses the <111>/2 screw, mixed and edge dislocation core structures and lattice frictions consistent with available DFT calculations and experimental observations in group VB TMs. Furthermore, V1 has relatively accurate twin boundary (TB) structures. Its mirror and isosceles TB energies are 0.316 and 0.314 J/m^2, 16% higher and 30% higher than the corresponding DFT values. Its twinning barrier γ_{utw} is 0.601 J/m^2, 2% higher than the DFT values. We have also used two more interatomic potentials (V2 and V3) for V to further validate the twin nucleation and growth mechanisms. V2 and V3 have largely similar properties as V1, but are tuned to possess different ΔE (SI). V1 and V2 exhibit the same twinning behaviour as shown in Fig. 5. Atomic configurations are visualized using the Open Visualization Tool (OVITO [69]).

Calculation of critical stress intensity factors

We consider a Griffith crack embedded in a large body under mode-I loading (Fig. 5a). The critical stress intensity factors (SIFs) can be calculated based on linear elastic fracture mechanics (LEFM) theory [70]. Specifically, the SIF for a crack of length $2a$ is

$$K_I = \sigma_0\sqrt{\pi a} \tag{2}$$

where σ_0 is the remote uniaxial loading in the *y*-direction. The SIF is modified for periodic array or doubly periodic arrays of cracks [71]. For example, when considering periodic boundary conditions along the x direction, the system simulates an array of cracks with image interactions. The corresponding SIF is

$$K_I^p = 2\sigma_0\sqrt{W}\frac{\sin\frac{\pi a}{2W}}{\sqrt{\sin\frac{\pi a}{W}}} = f(a,W)K_I \tag{3}$$

$$f(a,W) = \frac{\sqrt{6\pi a}(24W^2 - \pi^2a^2)}{24W\sqrt{6\pi aW^2 - \pi^3a^3}} \tag{4}$$

where $f(a, W)$ is a normalizing factor and W is the half width of the simulation cell. The factor $f(a, W)$ approaches 1 when $a/W < 0.1$. The image interaction effects are negligible when the ratio a/W is small, as in the current simulations.

For plane strain conditions, the critical SIF for cleavage is given by the Griffith theory [72] as

$$K_{Ic} = \sqrt{\frac{G}{D}} \tag{5}$$

where G is the energy release rate and equal to the energy required to create 2 surfaces, i.e., $2\sigma_{surf}$. The parameter D is related to the elastic constants

$$D = \frac{1-\nu^2}{E} \tag{6}$$

where ν is the Poisson's ratio and E is Young's modulus of the material, which can be obtained from the bulk modulus B and shear modulus μ as.

$$\nu = \frac{3B-2\mu}{2(3B+\mu)};\ E = \frac{9B\mu}{3B+\mu} \tag{7}$$

B and μ can be calculated from the 21 elastic constants by the Voigt-Reuss-Hill approximation [73]. For the cubic system,

$$B = \frac{B_R + B_V}{2} = \frac{C_{11}+2C_{12}}{3}(B_R = B_V);$$

$$\mu = \frac{\mu_R + \mu_V}{2};$$

$$\mu_R = \frac{5(C_{11}-C_{12})C_{44}}{4C_{44}+3(C_{11}-C_{12})}; \tag{8}$$

$$\mu_V = \frac{(C_{11}-C_{12}+3C_{44})}{5}.$$

The critical SIF for dislocation emission K_{Ie} can be calculated according to the Rice criterion [32]

$$K_{Ie} = \frac{1}{f(\theta)}\sqrt{\frac{2\mu}{1-\nu}[1+(1-\nu)\tan^2\phi]\gamma_{us}} \tag{9}$$

where $f(\theta) = \cos^2(\theta/2)\sin(\theta/2)$ and θ is the angle between the crack plane and slip plane, ϕ is the angle between the slip direction and the normal to crack front in the slip plane, and γ_{us} is the unstable

SF energy of the slip plane. In the γ_{rc}-lines, γ_{ud} better captures the barrier and can be used in place of γ_{us} in Eqn. (9). Similarly, the critical SIF for twinning nucleation K_{It} is calculated by replacing γ_{us} with γ_{utw} in Eqn. (9). We consider three crack orientations with dislocation and twin nucleation on the {112} plane as shown in Fig. S8. Table S4 shows all the material properties required in the above equations and Table S5 shows the respective predicted critical SIFs for 7 TMs. The above analysis is performed using isotropic linear elasticity, which yields values largely similar to that based on anisotropic linear elasticity [47].

Author contributions

JX designed the research and carried out the crack simulations. LZ and RW performed the DFT calculations. LZ carried out all continuum fracture mechanics calculations. RW developed the interatomic potentials for V. ZW and YZ wrote the paper. All authors analyzed the data and discussed the results.

CRediT authorship contribution statement

Jianwei Xiao: Conceptualization, Formal analysis, Investigation, Methodology, Writing – original draft. **Lingyu Zhu:** Formal analysis, Investigation, Methodology, Writing – original draft. **Rui Wang:** Formal analysis, Investigation, Methodology. **Chuang Deng:** Formal analysis, Resources, Writing – review & editing. **Zhaoxuan Wu:** Conceptualization, Formal analysis, Funding acquisition, Project administration, Supervision, Writing – original draft, Writing – review & editing. **Yuntian Zhu:** Project administration, Funding acquisition, Formal analysis, Supervision, Writing – review & editing.

Data availability

Data will be made available on request.

Declaration of Competing Interest

The authors declare that they have no known competing financial interests or personal relationships that could have appeared to influence the work reported in this paper.

Acknowledgments

This work is supported by the National Key R&D Program of China (2021YFA1200202), the Research Grants Council, Hong Kong SAR through the Early Career Scheme Fund (21205019) and the Collaborative Research Fund (8730054), and the National Natural Science Foundation of China (51931003). Computational resources are provided by Compute Canada and the Computing Services Centre, City University of Hong Kong.

Appendix A. Supplementary data

Supplementary data to this article can be found online at https://doi.org/10.1016/j.mattod.2023.03.028.

References

[1] B. Gludovatz et al., Science 345 (2014) 1153.
[2] J.W. Christian, S. Mahajan, Prog. Mater Sci. 39 (1995) 1.
[3] I.J. Beyerlein, X. Zhang, A. Misra, Annu. Rev. Mat. Res. 44 (2014) 329.
[4] G. Chen et al., Nat. Mater. 15 (2016) 876.
[5] B.C. De Cooman, Y. Estrin, S.K. Kim, Acta Mater. 142 (2018) 283.
[6] M. Marteleur et al., Materialia 7 (2019) 100418.
[7] T. Saito et al., Science 300 (2003) 464.
[8] A.T. Churchman, A.H. Cottrell, Nature 167 (1951) 943.
[9] D. Hull, Acta Metall. 9 (1961) 909.
[10] J. Edington, R. Smallman, Acta Metall. 13 (1965) 765–770.
[11] C.T. Wang, D.W. Bainbridge, Metall. Trans. 3 (1972) 3161–3165.
[12] S. Nemat-Nasser, W. Guo, Mech. Mater. 32 (2000) 243–260.
[13] Y.M. Wang et al., Appl. Phys. Lett. 86 (2005) 101915.
[14] B. Jiang et al., Acta Mater. 155 (2018) 56.
[15] R. Gröger et al., J. Mater. Res. 34 (2018) 261.
[16] J. Shields et al., Mater. Sci. Eng. 20 (1975) 71.
[17] J. Holzer et al., Int. J. Plast 138 (2021) 102938.
[18] B.J. Shaw, J. Less Common Met. 13 (1967) 294.
[19] C.V. Kopetskii, A.I. Pashkovskii, Phys. Status Solidi (a) 21 (1974) 741.
[20] H.-J. Kaufmann, A. Luft, D. Schulze, Cryst. Res. Technol. 19 (1984) 357.
[21] A. Argon, S. Maloof, Acta Metall. 14 (1966) 1449.
[22] X. Wang et al., Nat. Commun. 11 (2020) 2497.
[23] E.B. Tadmor, S. Hai, J. Mech. Phys. Solids 51 (2003) 765.
[24] S. Ogata, J. Li, S. Yip, Europhys. Lett. (EPL) 68 (2004) 405.
[25] S. Ogata, J. Li, S. Yip, Phys. Rev. B 71 (2005) 224102.
[26] P. Chowdhury, H. Sehitoglu, J. Eng. Mater. Technol. 140 (2018) 020801.
[27] J. Wang et al., J. Mater. Sci. Technol. 106 (2022) 33.
[28] A.H. Cottrell, B.A. Bilby, Science 42 (1951) 573.
[29] J.R. Morris et al., Philos. Mag. A 76 (1997) 1065.
[30] B. Yin, Z. Wu, W.A. Curtin, Acta Mater. 123 (2017) 223.
[31] V. Vítek, Phil. Mag. 18 (1968) 773.
[32] J.R. Rice, J. Mech. Phys. Solids 40 (1992) 239.
[33] Z. Wu et al., Acta Mater. 81 (2014) 428.
[34] W. Biggs, P. Pratt, Acta Metall. 6 (1958) 694.
[35] A. Hagen, B. Snartland, C. Thaulow, Acta Mater. 129 (2017) 398.
[36] I. Ringdalen Vatne et al., Mater. Sci. Eng. A 560 (2013) 306.
[37] G. Nouet, P. Delavignette, J. Microsc. Spectrosc. Electron 3 (1978) 389.
[38] R. Gröger, Z. Chlup, T. Kubenová, Mater. Sci. Eng. A 737 (2018) 413–421.
[39] J. Hirth, J. Lothe, *Theory of dislocations*, 2nd ed., Krieger Publishing Company, 1992.
[40] K. Ogawa, R. Maddin, Acta Metall. 12 (1964) 713.
[41] P. Raffo, J. Less Common Met. 17 (1969) 133.
[42] S. Mahajan, Phil. Mag. 26 (1972) 161.
[43] L. Bellaiche, D. Vanderbilt, Phys. Rev. B 61 (2000) 7877.
[44] Wang R., et al., arXiv: 10.48550/arXiv.2209.12323 (2022).
[45] P. Gumbsch et al., Science 282 (1998) 1293.
[46] J. Riedle, P. Gumbsch, H.F. Fischmeister, Phys. Rev. Lett. 76 (1996) 3594.
[47] E. Mak, B. Yin, W. Curtin, J. Mech. Phys. Solids 152 (2021) 104389.
[48] M.J. Witcomb et al., J. Mater. Sci. 3 (1968) 191.
[49] P. Flewitt, D. Palmer, J. Less Common Met. 32 (1973) 57.
[50] C. Reid, A. Gilbert, J. Less Common Met. 10 (1966) 77–90.
[51] P. Olsson et al., J. Nucl. Mater. 321 (2003) 84.
[52] C. Wang et al., Acta Mater. 215 (2021) 117094.
[53] G. Kanou et al., Mater. Trans. JIM 41 (2000) 197.
[54] K. Kako et al., Physica Status Solidi (a) 167 (1998) 481.
[55] J. Xie et al., Mater. Sci. Eng. A 538 (2012) 315.
[56] X. Shi et al., Mater. Sci. Eng. A 762 (2019) 138095.
[57] C. Han et al., J. Mater. Sci. Technol. 49 (2020) 25.
[58] J. Wang et al., Nat. Mater. 14 (2015) 594.
[59] L. Liu et al., Philos. Mag. Lett. 94 (2014) 225.
[60] Xiao J., et al., to be published (2023).
[61] G. Kresse, J. Furthmüller, Phys. Rev. B 54 (1996) 11169.
[62] G. Kresse, D. Joubert, Phys. Rev. B 59 (1999) 1758.
[63] J.P. Perdew, K. Burke, M. Ernzerhof, Phys. Rev. Lett. 77 (1996) 3865.
[64] P.E. Blöchl, Phys. Rev. B 50 (1994) 17953.
[65] M. Methfessel, A.T. Paxton, Phys. Rev. B 40 (1989) 3616.
[66] H.J. Monkhorst, J.D. Pack, Phys. Rev. B 13 (1976) 5188.
[67] A.P. Thompson et al., Comput. Phys. Commun. 271 (2022) 108171.
[68] R. Wang et al., Phys. Rev. Mater. 6 (2022) 113603.
[69] A. Stukowski, Model. Simul. Mater. Sci. Eng. 18 (2009) 015012.
[70] C.T. Sun, Z.H. Jin, *Fracture Mechanics*, 1st ed., Academic Press, 2011.
[71] B. Karihaloo, J. Wang, Mech. Mater. 26 (1997) 209.
[72] A.A. Griffith, Philos. Trans. R. Soc. Lond. A 221 (1921) 163.
[73] R. Hill, Proc. Phys. Soc. Sect. A 65 (1952) 349.